Journal of Solid State Chemistry 181 (2008) 1867–1875

Contents lists available at ScienceDirect

Journal of Solid State Chemistry

journal homepage: www.elsevier.com/locate/jssc

Magnetism and Raman spectroscopy of the dimeric lanthanide iodates $Ln(IO_3)_3$ (Ln = Gd, Er) and magnetism of $Yb(IO_3)_3$

Richard E. Sykora [a,*], Peter Khalifah [b,c], Zerihun Assefa [d], Thomas E. Albrecht-Schmitt [e], Richard G. Haire [f]

[a] Department of Chemistry, University of South Alabama, 307 University Blvd, Mobile, AL 36688-0002, USA
[b] Chemistry Department, Stony Brook University, Stony Brook, NY 11794, USA
[c] Chemistry Department, Brookhaven National Laboratory, Upton, NY 11973, USA
[d] Department of Chemistry, North Carolina A&T State University, Greensboro, NC 27411, USA
[e] Department of Chemistry and Biochemistry, Auburn University, Auburn, AL 36849, USA
[f] Chemical Sciences Division, Oak Ridge National Laboratory, Oak Ridge, TN 37831, USA

ARTICLE INFO

Article history:
Received 23 January 2008
Received in revised form
4 April 2008
Accepted 21 April 2008
Available online 1 May 2008

Keywords:
Gadolinium iodate
Erbium iodate
Ytterbium iodate
Hydrothermal synthesis
Single-crystal X-ray diffraction
Raman spectroscopy
Magnetic properties

ABSTRACT

Colorless single crystals of $Gd(IO_3)_3$ or pale pink single crystals of $Er(IO_3)_3$ have been formed from the reaction of Gd metal with H_5IO_6 or Er metal with H_5IO_6 under hydrothermal reaction conditions at 180 °C. The structures of both materials adopt the $Bi(IO_3)_3$ structure type. Crystallographic data are (Mo$K\alpha$, $\lambda = 0.71073$ Å): $Gd(IO_3)_3$, monoclinic, space group $P2_1/n$, $a = 8.7615(3)$ Å, $b = 5.9081(2)$ Å, $c = 15.1232(6)$ Å, $\beta = 96.980(1)°$, $V = 777.03(5)$ $Z = 4$, $R(F) = 1.68\%$ for 119 parameters with 1930 reflections with $I > 2\sigma(I)$; $Er(IO_3)_3$, monoclinic, space group $P2_1/n$, $a = 8.6885(7)$ Å, $b = 5.9538(5)$ Å, $c = 14.9664(12)$ Å, $\beta = 97.054(1)°$, $V = 768.4(1)$ $Z = 4$, $R(F) = 2.26\%$ for 119 parameters with 1894 reflections with $I > 2\sigma(I)$. In addition to structural studies, $Gd(IO_3)_3$, $Er(IO_3)_3$, and the isostructural $Yb(IO_3)_3$ were also characterized by Raman spectroscopy and magnetic property measurements. The results of the Raman studies indicated that the vibrational profiles are adequately sensitive to distinguish between the structures of the iodates reported here and other lanthanide iodate systems. The magnetic measurements indicate that only in $Gd(IO_3)_3$ did the 3+ lanthanide ion exhibit its full 7.9 μ_B Hund's rule moment; Er^{3+} and Yb^{3+} exhibited ground state moments and gap energy scales of 8.3 μ_B/70 K and 3.8 μ_B/160 K, respectively. $Er(IO_3)_3$ exhibited extremely weak ferromagnetic correlations (+0.4 K), while the magnetic ions in $Gd(IO_3)_3$ and $Yb(IO_3)_3$ were fully non-interacting within the resolution of our measurements (~0.2 K).

1. Introduction

The study of magnetic interactions in lanthanide complexes is currently an extremely active area of research [1–11]. In this regard, the most attention has been paid to materials that contain Gd^{3+} due to its $^8S_{7/2}$ ground state configuration, which is spherically symmetric. In contrast to transition metal systems, where magnetic interactions have been well understood for a number of years, the underlying mechanics governing the 4*f* systems are less resolved. For example, advances in recent years have shown that Gd–Gd coupling interactions in non-metallic compounds can be ferromagnetic [10], although earlier studies had found them to be only antiferromagnetic [11]. Since this discovery, the observation of *f*–*f* ferromagnetic coupling has been reported in a number of compounds, primarily in Gd^{3+} systems [8,12], but also in other lanthanide compounds [7,10]. The governing factors behind whether a material will display ferromagnetic or antiferromagnetic interactions are not well understood; however, recent spin density functional calculations have shown the difference is presumably between the open- and closed-shell electronic configurations, where the former generally lead to ferromagnetic interactions and the latter tend to prefer antiferromagnetic coupling [13].

Aside from the magnetic studies on *f*-element metallic and intermetallic-type phases [14,15], the vast majority of lanthanide complexes (insulating materials) that have been studied magnetically have two main features: (1) they contain organic bridging groups (e.g. carboxylate, N-oxide, etc.) between lanthanide centers and (2) they form low-dimensional magnetic structures [8–10,12]. Our interest lies in the study of inorganic *f*-element materials, and along these lines we have been studying the chemistry of the 4*f*- and 5*f*-element iodates.

The *f*-element iodates represent an extremely rich area of research, as evidenced by the large number of reports by us [16–21] and others [22–28]. Some of the main driving forces behind these studies are (1) the limited solubilities of iodates

* Corresponding author. Fax: +1 251 460 7359.
E-mail address: rsykora@jaguar1.usouthal.edu (R.E. Sykora).

0022-4596/$ - see front matter © 2008 Elsevier Inc. All rights reserved.
doi:10.1016/j.jssc.2008.04.019

which give them potential applications in separations and radioactive material deposition and (2) the potential for metal iodates to form non-centrosymmetric structures which give them potential applications in NLO, piezoelectricity, pyroelectricity, etc. The magnetism of the *f*-element iodates has been studied sparsely. Liminga et al. [26] have stated that the Gd^{3+} ions in Type I $Gd(IO_3)_3$ are non-interacting due to their large separation of 5.888 Å. Reports on the magnetic properties of trivalent 4*f*-ions doped in α-$LiIO_3$ [29] have shown that dimeric pairs of antiferromagnetic lanthanide (III) ions result in these materials. More recently, the magnetic interactions in an intermediate-valent cerium iodate system were reported [16]. This study revealed that the Ce ions in $Ce_2(IO_3)_6(OH_{0.44})$ are isolated and non-interacting.

The three iodates reported on here, Type II $Ln(IO_3)_3$ (Ln = Gd, Er, Yb), are all isostructural and structural data has been reported [17,23b]. It is important to note that the structures of these Type II anhydrous lanthanide iodates are quite different from that of the Type I anhydrous lanthanide iodates [26]. Due to the relatively short *Ln–Ln* distances (~4.2 Å) in the Type II iodates, our study was undertaken in order to probe whether any type of magnetic interactions may be observed in these compounds. Herein, we report on the magnetic properties of these compounds. In addition, a re-determination of the single-crystal X-ray structures (in order to deduce metal-metal separations) and Raman spectroscopy are reported for $Gd(IO_3)_3$ and $Er(IO_3)_3$.

2. Experimental

2.1. Materials and methods

Gd (Cerac, 99.9+%), Er (Cerac, 99.9+%), Yb (Cerac, 99.9+%), and H_5IO_6 (98%, Alfa-Aesar) were used as received without further purification. Triply distilled water was used as the solvent for all reactions. The reactions reported produced nearly quantitative yields of the respective compounds.

2.2. Synthesis of $Gd(IO_3)_3$, $Er(IO_3)_3$, and $Yb(IO_3)_3$

The synthesis of $Gd(IO_3)_3$ involved loading Gd (3.059 mg, 19.5 μmol) and H_5IO_6 (13.319 mg, 58.4 μmol) in a quartz reaction vessel followed by the addition of distilled water (100 μL). The reaction vessel was then sealed, placed in a furnace, and then heated to 180 °C where the reaction/crystallization occurred under autogenously generated pressure. After 70 h, the furnace was turned off and allowed to self-cool to 20 °C. The product mixture included colorless crystals of $Gd(IO_3)_3$ in a colorless mother liquor. The synthesis of $Er(IO_3)_3$ was similar to the synthesis of $Gd(IO_3)_3$ except that Er (4.133 mg, 24.7 μmol) and H_5IO_6 (16.710 mg, 73.3 μmol) were used in the reaction. The reaction was carried out for 64 h, after which time the furnace was turned off and allowed to self-cool to 20 °C. The product mixture included pink crystals of $Er(IO_3)_3$ in a colorless mother liquor. The synthesis of $Yb(IO_3)_3$ was conducted as reported in the literature [17].

2.3. Crystallographic studies

Selected single crystals of $Gd(IO_3)_3$ and $Er(IO_3)_3$ with dimensions of 0.126 mm × 0.044 mm × 0.042 mm and 0.186 mm × 0.120 mm × 0.069 mm, respectively, were selected, mounted on fibers, and aligned on a Bruker SMART APEX CCD X-ray diffractometer with a digital camera. Intensity measurements were performed using graphite monochromated Mo*K*α radiation from a sealed tube with a monocapillary collimator. The intensities and positions of reflections of a sphere were collected by a combination of three sets of exposure frames. Each set had a different φ angle for the crystal and each exposure covered a range of 0.3° in ω. A total of 1800 frames were collected with an exposure time per frame of 20 s for both crystals.

Crystals of $Gd(IO_3)_3$ and $Er(IO_3)_3$ diffracted extremely well and were non-problematic in regards to data collection and structure analysis. Determination of integrated intensities and global cell refinement were performed with the Bruker SAINT (v 6.02) software package using a narrow-frame integration algorithm. A face-indexed absorption correction was applied followed by a semi-empirical absorption correction using SADABS [30]. The program suite SHELXTL (v 5.1) was used for space group determination (XPREP), direct methods structure solution (XS), and least-squares refinement (XL) [31]. The final refinement included anisotropic displacement parameters for all atoms and a secondary extinction parameter. Additional crystallographic details are listed in Table 1 and the final positional parameters can be found in Tables 2 and 3. Further details of the crystal structure investigations may be obtained from the Fachinformationzentrum Karlsruhe, 76344 Eggenstein-Leopoldshafen, Germany (fax: +49 7247 808 666; e-mail: crysdata@fiz-karlsruhe.de, http://www.fiz-karlsruhe.de/request_for_deposited_data.html) on quoting the depository numbers CSD 418522, 418521, and 416690 for $Gd(IO_3)_3$, $Er(IO_3)_3$, and $Yb(IO_3)_3$, respectively.

2.4. Raman spectroscopy

Raman spectra were obtained at room temperature on crystalline samples using an argon-ion laser (Coherent, model 306) and a double-meter spectrometer (Jobin-Yvon Ramanor model HG.2S). The resolution of the monochromator is 0.5 cm^{-1}. The monochromator is interfaced with a personal computer; scanning and data collections are controlled by LabSpec (version 3.04) software. Signal detection was with a water-cooled photo-multiplier tube (Hamamatsu R636).

2.5. Magnetic measurements

Magnetization measurements were conducted on wrapped polycrystalline samples mounted inside a clear plastic straw,

Table 1
Crystallographic data for $Gd(IO_3)_3$ and $Er(IO_3)_3$

Formula	$Gd(IO_3)_3$	$Er(IO_3)_3$
Formula mass	681.95	691.96
Color	Colorless	Pale pink
Crystal system	Monoclinic	Monoclinic
Space group	$P2_1/n$ (no. 14)	$P2_1/n$ (no. 14)
a (Å)	8.7615(3)	8.6885(7)
b (Å)	5.9081(2)	5.9538(5)
c (Å)	15.1232(6)	14.9664(12)
β	96.980(1)	97.054(1)
V (Å^3)	777.03(5)	768.35(11)
Z	4	4
T (K)	173	173
λ (Å)	0.71073	0.71073
$2\theta_{max}$ (deg)	56.62	56.58
ρ_{calcd} (g/cm^3)	5.829	5.982
μ(Mo*K*α) (cm^{-1})	20.479	23.001
Reflections collected	7657	7230
Independent reflections	1930 [R(int) = 0.0215]	1894 [R(int) = 0.0376]
Data/restraints/parameters	1930/0/119	1894/0/119
$R(F)$ for $F_o^2 > 2\sigma(F_o^2)$[a]	0.0168	0.0226
$R_w(F_o^2)$[b]	0.0398	0.0567

[a] $R(F) = \sum ||F_o| - |F_c|| / \sum |F_o|$.
[b] $R_w(F_o^2) = [\sum[w(F_o^2 - F_c^2)^2] / \sum wF_o^4]^{1/2}$.

Table 2
Atomic coordinates and equivalent isotropic displacement parameters for $Gd(IO_3)_3$

Atom	Site	x	y	z	U_{eq} (Å^2)[a]
Gd1	4e	0.5409(1)	0.7267(1)	0.8991(1)	0.008(1)
I1	4e	0.8345(1)	0.3568(1)	0.9780(1)	0.007(1)
I2	4e	0.6175(1)	0.4072(1)	0.6986(1)	0.007(1)
I3	4e	0.2799(1)	0.1870(1)	0.8518(1)	0.007(1)
O1	4e	0.7788(3)	0.5309(5)	0.8805(2)	0.010(1)
O2	4e	0.3604(4)	0.6081(5)	0.9908(2)	0.012(1)
O3	4e	0.9112(3)	0.5794(5)	0.0555(2)	0.011(1)
O4	4e	0.5866(4)	0.6841(5)	0.7439(2)	0.010(1)
O5	4e	0.4535(4)	0.4106(6)	0.6134(2)	0.014(1)
O6	4e	0.7693(4)	0.4991(5)	0.6335(2)	0.011(1)
O7	4e	0.3615(4)	0.9440(6)	0.8008(2)	0.013(1)
O8	4e	0.3613(4)	0.0998(5)	0.9625(2)	0.012(1)
O9	4e	0.4228(4)	0.3960(5)	0.8291(2)	0.011(1)

[a] U_{eq} is defined as one-third of the trace of the orthogonalized U_{ij} tensor.

Table 3
Atomic coordinates and equivalent isotropic displacement parameters for $Er(IO_3)_3$

Atom	Site	x	y	z	U_{eq} (Å^2)[a]
Er1	4e	0.5425(1)	0.7171(1)	0.8966(1)	0.008(1)
I1	4e	0.8332(1)	0.3519(1)	0.9788(1)	0.007(1)
I2	4e	0.6181(1)	0.4045(1)	0.6985(1)	0.007(1)
I3	4e	0.2802(1)	0.1877(1)	0.8549(1)	0.007(1)
O1	4e	0.7741(5)	0.5290(8)	0.8816(3)	0.010(1)
O2	4e	0.3622(5)	0.6239(8)	0.9889(3)	0.013(1)
O3	4e	0.9102(5)	0.5675(8)	0.0589(3)	0.011(1)
O4	4e	0.5860(5)	0.6817(7)	0.7438(3)	0.010(1)
O5	4e	0.4557(5)	0.4131(8)	0.6104(3)	0.014(1)
O6	4e	0.7751(5)	0.4937(7)	0.6359(3)	0.010(1)
O7	4e	0.3675(5)	0.9424(8)	0.8095(3)	0.012(1)
O8	4e	0.3543(5)	0.1195(8)	0.9698(3)	0.013(1)
O9	4e	0.4223(5)	0.3963(8)	0.8296(3)	0.011(1)

[a] U_{eq} is defined as one-third of the trace of the orthogonalized U_{ij} tensor.

using a superconducting quantum interference device (SQUID) magnetometer, over the temperature range 2–300 K at a sweep rate of 1 K/min. By collecting magnetic data continuously during field sweeps, a greater density of data points could be collected, allowing improved fits to the data. One side effect of this procedure was the introduction of a slight temperature offset, which has typically led to a 0.2 K difference between data collected on heating and on cooling. Both zero-field-cooled (ZFC) and field-cooled (FC) DC susceptibility measurements were made under applied fields of 0.1 and 5 T, with the ZFC data collected on heating and the FC data collected on cooling. Magnetization versus applied fields up to 5 T was measured at 5 K.

3. Results and discussion

3.1. Syntheses

The syntheses of $Gd(IO_3)_3$ and $Er(IO_3)_3$ are very straightforward. These compounds have been prepared by reacting the appropriate lanthanide metal with periodic acid under hydrothermal conditions (180 °C) for several days; this synthetic procedure is similar to the one employed for the synthesis of $Yb(IO_3)_3$ [17]. The anhydrous iodates are recovered from these reactions in nearly quantitative yields. This synthetic procedure is different from that previously reported for $Gd(IO_3)_3$ and $Er(IO_3)_3$ [23b], where lanthanide nitrate or chloride salts were reacted with iodic acid. It was reported that the isostructural $Yb(IO_3)_3$ could not be formed by starting with the nitrate or chloride salts [23b], although it was isolated following oxidation of Yb metal with periodic acid [17].

3.2. Structures of $Ln(IO_3)_3$ (Ln = Gd, Er, Yb)

Since all three compounds are isostructural, they will be discussed together for brevity; all three structures have been reported previously [17,23b], but a short description is warranted here to aid in the understanding of the Raman and magnetic discussions. The structures reported for $Gd(IO_3)_3$ and $Er(IO_3)_3$ in the literature were refined with data that was only measured to a maximum Theta of 21.4°; therefore, we concluded that a re-determination of the crystal structures was warranted. All of these compounds contain the $Bi(IO_3)_3$ structure type [32]. It has also been shown that many other lanthanide [17,23b,33] and actinide iodates [20,24], including $Cf(IO_3)_3$, crystallize in this structure type. The unique lanthanide crystallographic position in the structure is coordinated in its inner sphere by oxygen atoms from three crystallographically unique iodate anions. Each of these iodate anions is composed of a central iodine atom surrounded by three oxygen atoms in a trigonal pyramidal arrangement, and also contains a lone pair of electrons. Seven short Gd–O (Er–O) contacts ranging from 2.334(3) to 2.442(3) Å (2.280(4) to 2.377(4) Å) are present for each lanthanide with two longer contacts of 2.662(3) and 2.936(3) Å (2.720(5) and 3.170(5) Å) resulting in a total coordination environment of nine. While these two long bond distances are significantly longer than the remaining Ln–O distances, they are short enough to be significant, as evidenced from their bond valence contributions [34] of 0.20 and 0.09 for $Gd(IO_3)_3$ and 0.15 and 0.04 for $Er(IO_3)_3$. As shown in Fig. 1, the oxygen atoms are arranged in distorted tricapped trigonal prismatic coordination environments, with the two long contacts filling two of the capping positions.

The LnO_9 polyhedra share edges to form one-dimensional chains (Fig. 1) that are parallel to the crystallographic *b* axis. Alternating short and long Ln–Ln distances, e.g. 4.187 and 4.559 Å for $Gd(IO_3)_3$, (4.167 and 4.693 Å for $Er(IO_3)_3$ and 4.220 and 4.706 Å for $Yb(IO_3)_3$) are found in these chains. The ramifications of these alternating distances on the magnetic properties of these compounds are described later. In addition to the edge-sharing interactions between LnO_9 polyhedra, $I1O_3^-$ and $I3O_3^-$ anions further bind the LnO_9 polyhedra together as shown in Fig. 2 into two-dimensional structural sheets.

The iodate anions each have three short bond lengths ranging from 1.806(3) to 1.838(3) Å for $Gd(IO_3)_3$ (1.807(4) to 1.827(4) for $Er(IO_3)_3$), well within the ranges found for other iodates [35–37]. The iodate anion formed from I1 can be described as an IO_{3+1} anion resulting from the coordination of three short I–O bonds and one lengthened distance of 2.375 Å in $Gd(IO_3)_3$ (2.420 Å in $Er(IO_3)_3$). Table 4 gives a brief listing of relevant bond lengths for the representative compound, $Gd(IO_3)_3$. Detailed lists of bond lengths and angles for $Ln(IO_3)_3$ (*Ln* = Gd, Er, Yb) can be obtained from the Fachinformationzentrum Karlsruhe (contact information given in Section 2).

3.3. Vibrational spectroscopy

In Fig. 3, the Raman spectra of $Er(IO_3)_3$ and $Gd(IO_3)_3$ are shown in the ν_{I-O} stretching frequency region. Consistent with the structural similarities of the two compounds, the Raman profiles are somewhat similar in both energy positions and relative intensities of the peaks. In the ν_{I-O} symmetric stretching region, the Raman spectrum of $Er(IO_3)_3$ exhibits three main bands: a strong doublet at 700 and 724 cm^{-1}, a broad doublet at 766 and 782 cm^{-1}, and a strong band at 829 cm^{-1}. Cooling the sample to

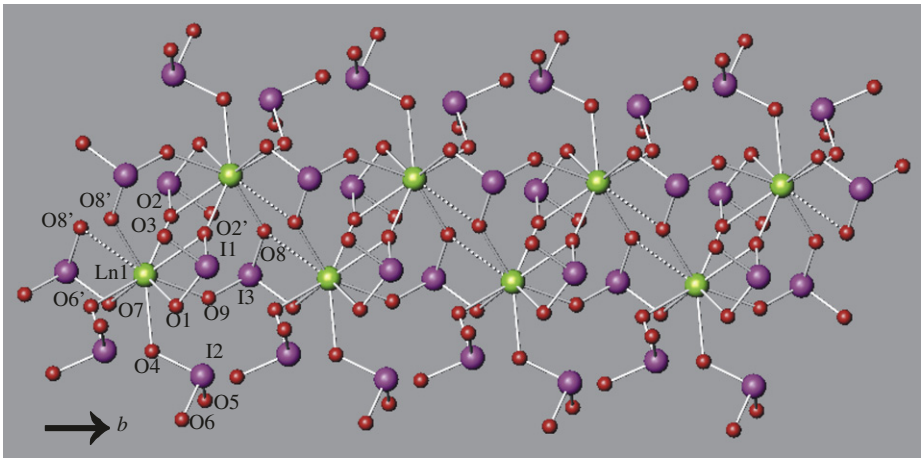

Fig. 1. A representation of the chains in the structure of $Ln(IO_3)_3$ (Ln = Gd, Er, Yb). The dashed lines indicate the two longest Ln–O contacts. The shorter Ln–Ln contact is created by the bridging O2 atoms (50% probability ellipsoids are shown).

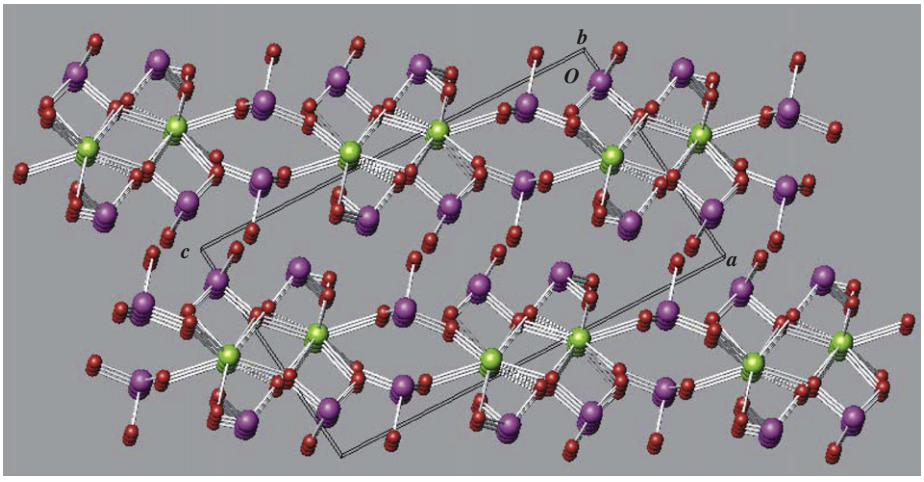

Fig. 2. A packing diagram viewed along the b-axis showing the stacking of the two-dimensional layers in $Ln(IO_3)_3$ (Ln = Gd, Er, Yb).

Table 4
Selected bond distances (Å) for $Gd(IO_3)_3$

Gd1–O1	2.430(3)	I1–O1	1.815(3)
Gd1–O2	2.334(3)	I1–O2a	1.838(3)
Gd1–O2a	2.662(3)	I1–O3d	1.835(3)
Gd1–O4	2.442(3)	I2–O4	1.806(3)
Gd1–O6b	2.408(3)	I2–O5	1.810(3)
Gd1–O7	2.400(3)	I2–O6	1.831(3)
Gd1–O8a	2.394(3)	I3–O7e	1.817(3)
Gd1–O8c	2.936(3)	I3–O8	1.813(3)
Gd1–O9	2.397(3)	I3–O9	1.821(3)
Gd1–Gd1a	4.187	Gd1–Gd1f	4.559

Symmetry codes: (a) 1−x, 1−y, 2−z; (b) 1.5−x, 1/2+y, 1.5−z; (c) x, 1+y, z; (d) x, y, 1+z; (e) x, y−1, z; (f) 1−x, 2−y, 2−z.

liquid N_2 temperature resulted in only minor changes, with the main consequence being the splitting of the broad band at 724 nm into three components (718, 734, and 745 cm^{-1}). Compared with the room temperature spectrum, the band at 696 cm^{-1} in the low-temperature spectrum is red-shifted by about 4 cm^{-1}.

The spectrum of $Gd(IO_3)_3$ is shown in Fig. 3c and exhibits a similar profile with peaks at 699, 730, 761, 782, and a broad doublet at 803 and 813 cm^{-1}. Although, the overall spectral profile of the two complexes are similar, the highest vibrational band at 829 cm^{-1} in $Er(IO_3)_3$ is red shifted to 813 cm^{-1} for $Gd(IO_3)_3$. Similar vibrational profiles were observed for $Cf(IO_3)_3$ [20], $Lu(IO_3)_3$ [17], and $Yb(IO_3)_3$ [17] which also have the $Bi(IO_3)_3$ structure type.

Compared with the ~770 cm^{-1} average ν_{I-O} frequency reported for iodate salts of mono- and divalent cations [38,39], or to the ~785 cm^{-1} frequency assigned to the symmetric stretching mode in actinyl iodates [40], higher frequency bands of up to 840 cm^{-1} distinguish the trivalent f-element iodates, as has been the case in $Cm(IO_3)_3$ [19], $Cf(IO_3)_3$ [20], and $Lu(IO_3)_3(H_2O)$ [17]. With the present structural morphology in $Er(IO_3)_3$ and $Gd(IO_3)_3$, the highest ν_{I-O} stretching bands are located at 829 and 813 cm^{-1}, respectively. As reported recently by us, $Cf(IO_3)_3$, $Yb(IO_3)_3$, and $Lu(IO_3)_3$, which crystallize with the same structure type, have their highest I–O vibrational band at a similar frequency and exhibit similar spectral profiles [17,20]. When compared with other actinide and lanthanide iodates with different structural features, the Raman spectra of $Er(IO_3)_3$ and $Gd(IO_3)_3$ reported here have an overall different spectral profile. For example, the Type I trivalent iodates $Nd(IO_3)_3$, $Am(IO_3)_3$, [18] and $Cm(IO_3)_3$ [18,19], which are not isostructural with the $Gd(IO_3)_3$ and $Er(IO_3)_3$ structures reported here, show a distinctly different vibrational profile. Thus, the Raman probe is adequately sensitive to distinguish between the different types of structural features.

Previous interpretations of Raman spectra corresponding to the ν_{I-O} vibrations in iodate salts of trivalent lanthanide and actinide systems are based on the assumption that little inter-ionic coupling exists between the crystallographically unique IO_3^- anions [17–20,36]. As with anhydrous $Yb(IO_3)_3$ [17], the presence of three distinct iodate ions is a characteristic feature in both $Er(IO_3)_3$ and $Gd(IO_3)_3$. Hence, each of the spectral regions described above can be associated with the unique iodate anions.

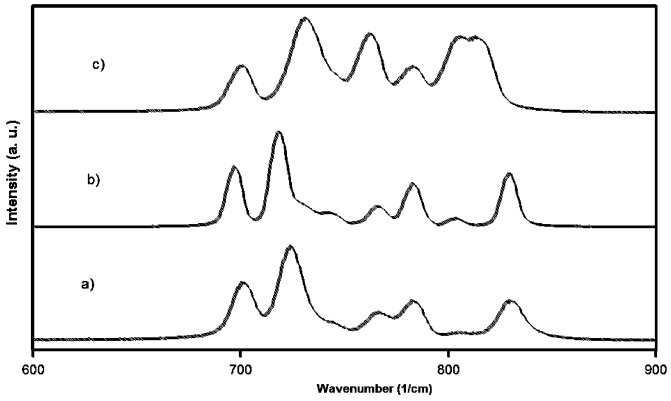

Fig. 3. Raman spectra in the ν_{I-O} stretching region of (a) $Er(IO_3)_3$ at room temperature, (b) $Er(IO_3)_3$ at liquid N_2 temperature, and (c) $Gd(IO_3)_3$ at room temperature. These spectra were collected using the 514.5 nm argon laser line.

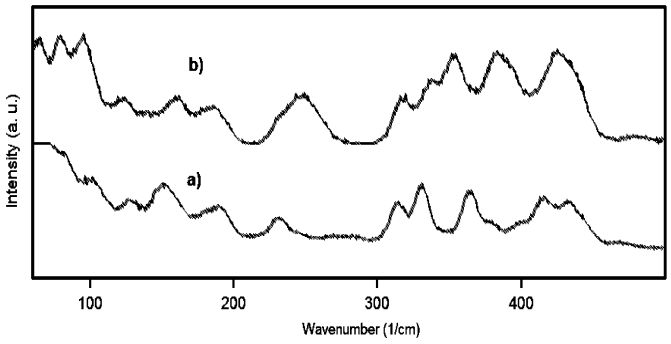

Fig. 4. Raman spectra in the O–I–O bending and lattice mode region for (a) $Er(IO_3)_3$, (b) $Gd(IO_3)_3$. Both spectra were collected at room temperature using the 514.5 nm argon laser line.

However, for each unique iodate ion the presence of intra-ionic vibrational coupling is dependent on several factors. Previous studies of iodate salts of mono- and divalent cations revealed that when one of the I–O bond distances in an iodate anion is significantly shorter than the other two distances, an uncoupled symmetric stretching mode is displayed [38,39]. In such instances, the asymmetric component appears at a lower energy compared with the symmetric stretching frequency. An intensity comparison can also help to differentiate between these two modes, as the symmetric component usually displays a more intense band than the asymmetric component. For $Gd(IO_3)_3$ and $Er(IO_3)_3$, each of the three spectral regions show the presence of weak shoulders and/or components both on the high- and low-energy sides of the most intense bands, which suggests intra-ionic coupling exists. The I–O bond distances at the three unique sites are essentially indistinguishable having average values of 1.824, 1.819, and 1.815 Å at the I1, I2, and I3 sites, respectively. However, the average O–I–O angle at the I1 site is smaller compared with the other two sites (93.7, 97.1, and 97.4 at the I1, I2, and I3 sites, respectively).

Following previous suggestions [41,42], it can be argued that the smaller O–I–O angle at the I1 site induces a higher frequency shift to the I–O symmetric stretching mode. Hence, the band at 829 cm^{-1} in $Er(IO_3)_3$ or at 813 cm^{-1} in $Gd(IO_3)_3$ can be assigned to this site. Correlating this with previous data, we conclude that as the Ln^{3+} cation size in the structure increases, the frequency of the highest energy band decreases, e.g. the highest energy band occurs at 842 and 840 cm^{-1} in $Lu(IO_3)_3$ and $Yb(IO_3)_3$, respectively [17].

The region covering the low energy O–I–O bending modes is shown in Fig. 4a for the $Er(IO_3)_3$ system. Following previous assignments [17,36], the Raman modes below 300 cm^{-1} are assigned to lattice modes. In the 300–500 cm^{-1} region there are a total of seven well-defined bands at 312, 330, 363, 379, 398, 414, and 433 cm^{-1}, while the lattice modes are observed at 82, 103, 126, 150, 189, 231, and 278 cm^{-1}. Similarly, the $Gd(IO_3)_3$ system shows bands assignable to the O–I–O bending modes at 316, 330, 352, 385, and 430 cm^{-1} and the lattice modes consist of bands at 65, 79, 94, 124, 158, and 185 cm^{-1}.

3.4. Magnetic properties

Because these compounds are highly insulating, it is expected that the magnetic interactions between the lanthanide ions will

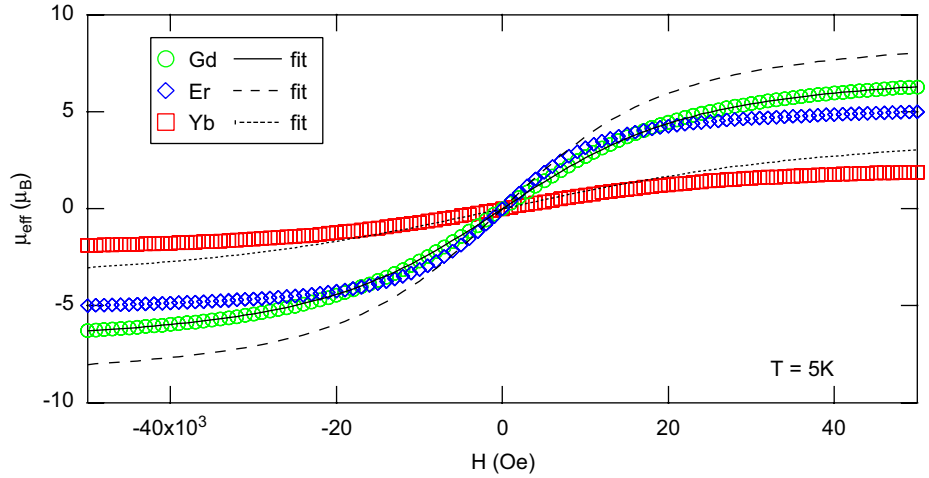

Fig. 5. Field-dependent magnetization curves at 5 K. The magnetization curve of Gd^{3+} is well-described by a Brillouin function ($g = 2$, $J = 3.5$), while the curves of Er^{3+} ($g = 1.2$, $J = 7.5$) and Yb^{3+} ($g = 8/7$, $J = 3.5$) exhibit a substantially reduced magnetization relative to the Brillouin function predictions.

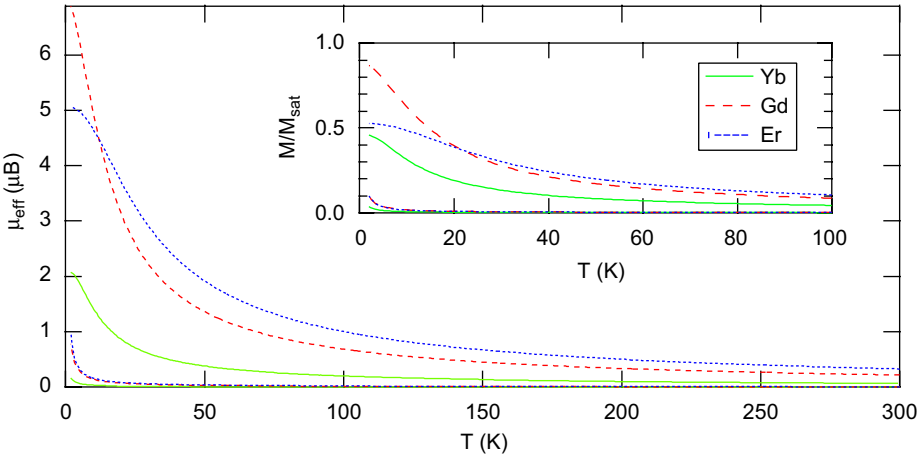

Fig. 6. Magnetic moments and degree of saturation for $Gd(IO_3)_3$, $Er(IO_3)_3$, and $Yb(IO_3)_3$. Upper set of lines are data collected at $H = 50$ kOe (5 T), while lower set of lines represents data at $H = 1$ kOe (0.1 T).

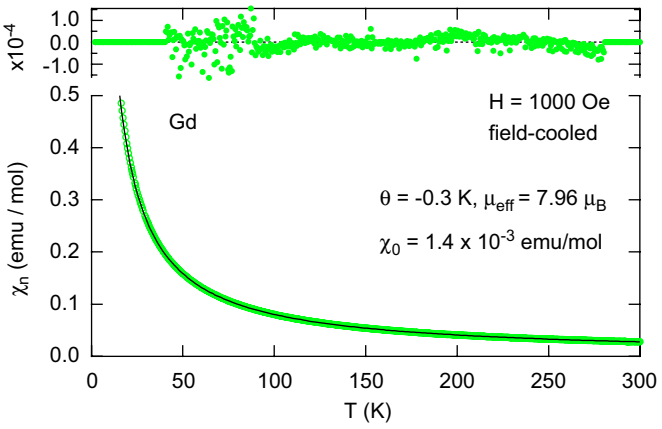

Fig. 7. Temperature-dependent molar susceptibility of $Gd(IO_3)_3$. Predictions (solid line) and residuals (top) are from a modified Curie–Weiss law fit from 40 to 280 K.

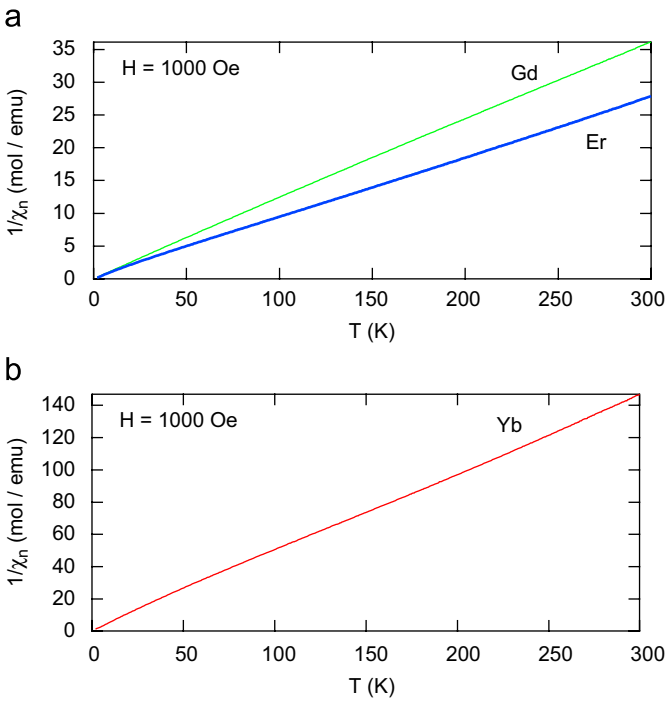

Fig. 8. Inverse molar susceptibility of (a) $Gd(IO_3)_3$ and $Er(IO_3)_3$, and (b) $Yb(IO_3)_3$ measured at an applied field of 1000 Oe. The multiple inflection points of the Yb and Er samples are a signature of the thermally varying population of the excited crystal field levels.

be weak, since the RKKY mechanism [43] will not operate in the absence of mobile electrons. The effective moments (μ_{eff}) for the ideal ground state configurations of these ions are determined by Hund's rules, which predict a moment of 7.94 μ_B for Gd^{3+} ($4f^7$, $^8S_{7/2}$ ground state), 9.58 μ_B for Er^{3+} ($4f^{11}$, $^4I_{15/2}$), and 4.54 μ_B for Yb^{3+} ($4f^{13}$, $^2F_{7/2}$). However, the magnetism of Er^{3+} and Yb^{3+} compounds are strongly influenced by the crystal fields of the ligands, and will generally exhibit a temperature-dependent reduction of their effective moments from the lifting of the ground state degeneracy, and the reduced magnetism of the resulting Stark levels [44]. The Gd^{3+} compound has an $L = 0$ ground state, and is therefore not susceptible to crystal field effects and should manifest its full Hund's rule moment. This is demonstrated in Fig. 5, where the 5 K magnetization of the Gd^{3+} compound closely follows the ideal behavior described by a Brillouin function, while the Er^{3+} and Yb^{3+} compounds do not.

As seen in Fig. 5, the compounds are nearly magnetically saturated at low temperatures and high fields. In the analysis of these materials, it is important to know exactly when saturation effects become significant. Fig. 6 shows the temperature-dependent magnetization of these compounds in units of μ_B. It can be seen that the high-field ($H = 50$ kOe) magnetization of the Er^{3+} and Yb^{3+} compounds begin to flatten well below the saturation moment predicted by Hund's rules, again highlighting the role that crystal field splitting plays in reducing the net magnetization of these compounds. Even at room temperature, all three compounds have developed a significant fraction (1–3%) of their Hund's rule moment when measured under the high-field conditions. At the minimum temperature (2 K) and under low fields conditions ($H = 1000$ Oe), the Gd^{3+} and Er^{3+} compounds are at about 10% of their Hund's rule moment, while Yb^{3+} is only at 4% saturation. Since the compounds exhibit nearly Curie-like behavior ($\chi \sim C/T$), the degree of saturation will be halved each time the temperature is doubled. While the low-T/low-H magnetizations are slightly higher than desired, saturation effects will be small even in this regime, and should be negligible by 20 K, where the samples are at about 0.5% of their saturation moment. Any

saturation effects will result in the samples appearing to have slightly more antiferromagnetic correlations than their intrinsic behavior.

Based on the crystal structures of these compounds, there are only two possible types of magnetic behaviors that can be expected from the Ln^{3+} ions, namely coupled dimers or free ions. It is possible that there will be significant magnetic exchange interactions through the two bridging oxygens between dimeric pairs of nearest-neighbor (d~4.2 Å) Ln^{3+} ions. These are the only Ln^{3+} sites that can be reasonably expected to interact, since the other pairs of Ln^{3+} sites have far greater separation distances (d>4.5 Å) and will not have a measurable degree of magnetic coupling. Alternatively, if the dimeric Ln^{3+}–Ln^{3+} coupling is negligible, the magnetism of these compounds will just be that of free Ln^{3+} ions (but modified by the local crystal fields in the case of Er^{3+} and Yb^{3+}).

We can use the Gd^{3+} compound to distinguish between these two possibilities. In the simple free-ion picture, the S-state Gd^{3+} should behave as a simple Curie–Weiss paramagnet. [$\chi \propto C/(T-\theta)$] with θ being very small or zero. Fig. 7 shows its FC low-field ($H = 1000$ Oe) magnetic susceptibility data and its least-squares fit to a modified Curie–Weiss law [$\chi = \chi_0 + C/(T-\theta)$] in the range of 40–280 K. The validity of this model can be seen by its small residuals, and in a $1/\chi_m$ plot (Fig. 8a), which only shows a slight bending away from linearity due to the constant background term, χ_0. The best fit parameters indicate $\theta = -0.3$ K and $\mu_{eff} = 7.96\,\mu_B$. Although the fit is quite good (root mean square error $= 3.6 \times 10^{-5}$ emu/mol), there is still significant uncertainty in θ due to the very high degree of cross-correlation ($\theta/C = -0.97$, $\theta/\chi_0 = 0.89$; $C/\chi_0 = -0.95$) between parameters. If the influence of the correlations are minimized by constraining the fit to have the ideal Gd^{3+} moment of 7.94 μ_B, the resulting fit gives $\theta = -0.1$ K,

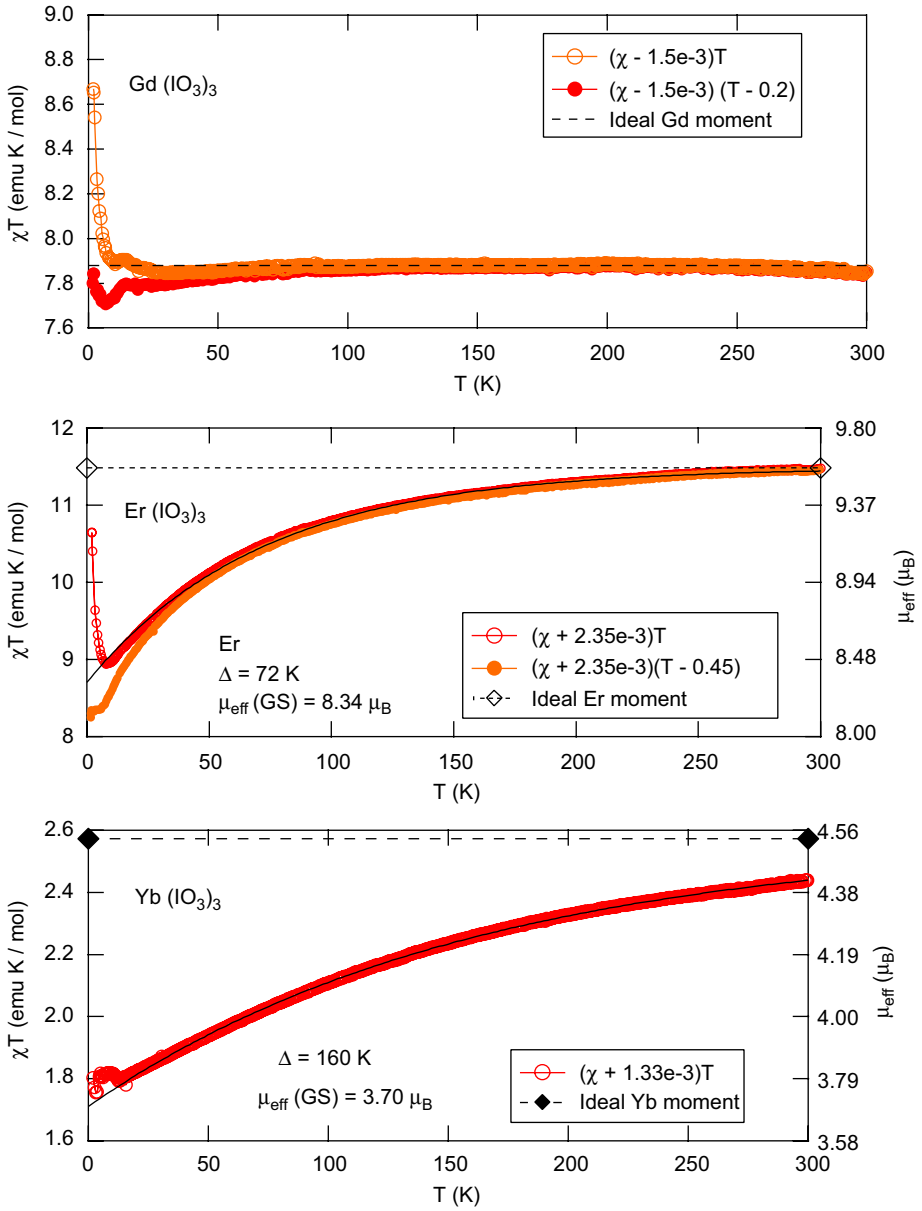

Fig. 9. χT plots, showing the temperature dependence of $Ln(IO_3)_3$ effective moments. Data have been corrected for a temperature independent background, and in the case of Gd^{3+} and Er^{3+}, also for a temperature shift. While Gd^{3+} shows its ideal Hund's rule moment, Er^{3+} and Yb^{3+} show reduced moments whose complex temperature dependence is roughly described by a simple two-parameter fit. The ground state moment and global crystal field gap, Δ, were obtained by a fit of the form $\chi T = \chi T_{full} + A\exp(-\Delta/T)$, where $A = \chi T_{full} - \chi T_{GS}$ and "full" and "GS" indicates the values for the full moment of Hund's rule prediction and the reduced moment of the crystal field ground state, respectively. As is commonly found in the literature, Yb^{3+} has a substantially larger crystal field splitting than Er^{3+}.

strongly suggesting that the nearest-neighbor Gd^{3+} ions are magnetically decoupled, and are behaving as free ions. The field-dependent magnetization of this compound measured at 5 K (Fig. 5) does not show significant deviation from a Brillouin function, also supporting the free-ion model.

Despite the crystal field effects, the inverse susceptibility data for Er^{3+} and Yb^{3+} still exhibit a nearly-linear temperature dependence (Fig. 8), though the multiple inflection points in these plots were a clear sign that the Curie–Weiss law cannot be readily applied to these materials. Closer insights into the crystal field effects could be obtained by looking at the χT product of these compounds, which will be proportional to the local moment, μ_{eff}, at all temperatures if the magnetic susceptibility follows a simple Curie law behavior ($\chi = C/T$). For these samples, this is a good starting approximation, though it should be noted that the χ_0 offset (from the temperature-independent sample holder background and elemental Larmor diamagnetism) may cause appreciable deviations at high T, and temperature errors (both due to the sweeping measurement program and thermometer calibration errors) will cause substantial errors at low T.

We have attempted to estimate and correct for the χ_0 offset by subtracting a value of χ_0 that leads to the compounds exhibiting their full moment of their Hund's rule ground state. While this was relatively straightforward for Gd^{3+}, for Er^{3+} and Yb^{3+} χ_0 was chosen so that a fit to an exponential function of the form $(\chi T) = (\chi T)_0 - A\exp(\Delta/T)$, Fig. 9, returns a value $(\chi T)_0$ that matches the χT product predicted for Hund's rule ground state of the ion, a value that should be recovered experimentally at high temperatures (relative to the crystal field gaps). This fit function very roughly approximates the multi-level manifold of the crystal field levels, and gives a sense of the magnitude of the crystal field splitting even in the absence of the detailed information necessary for an analytical fit, namely, the number of levels (typically 8 for Er^{3+} and 4 for Yb^{3+}), their degeneracy, their energies, and their effective moments. From our fits, we obtain a "global" gap splitting of 72 K for Er^{3+} and 160 K for Yb^{3+}, consistent with prior studies on these ions in other environments [45–51], which have found substantially smaller gaps for Er^{3+} than Yb^{3+}. Also, it allows us to estimate the ground state effective moment of Er^{3+} as 8.34 μ_B and that of Yb^{3+} as 3.70 μ_B, though these numbers are expected to be slightly lower than their true values since the exponential fit function applied here does not flatten out at low temperatures where only the ground state crystal field level(s) are populated.

A second estimate of the ground state moment can be obtained by fitting the low-temperature molar susceptibility data to a Curie–Weiss law (Fig. 10). Since the first excited crystal field level typically has a gap of 30–90 K for Er^{3+} and 200–700 K for Yb^{3+}, it is generally possible to measure magnetic susceptibilities down to temperatures where only the ground state crystal field level is occupied. Empirically, "low" temperatures are those where the inverse susceptibility data are linear to the lowest measurable temperature of 2 K. It should be noted that the temperature-independent background susceptibility is very small relative to the magnetic response of the samples at these temperatures, so deviations from linearity are almost certainly a sign of changing populations of the crystal field levels. These values (8.26 μ_B for Er^{3+}, and 3.81 μ_B for Yb^{3+}) are in good agreement with the values obtained from the exponential fits (8.34 μ_B for Er^{3+}, and 3.70 μ_B for Yb^{3+}), demonstrating that these estimates of the ground state moment are quite reasonable.

Additionally, these low-T fits give us a window into the nature of the magnetic interactions of these Ln^{3+} ions in their ground states. While the slight deviations of θ from zero ($\theta_{Gd} = +0.1$ K, T_{offset} in χT plot $= +0.2$ K) for Gd^{3+} are most likely attributable to the slight temperature offset from collecting magnetic data in a "sweep" mode instead of a "settle" mode, the larger θ for Er^{3+}

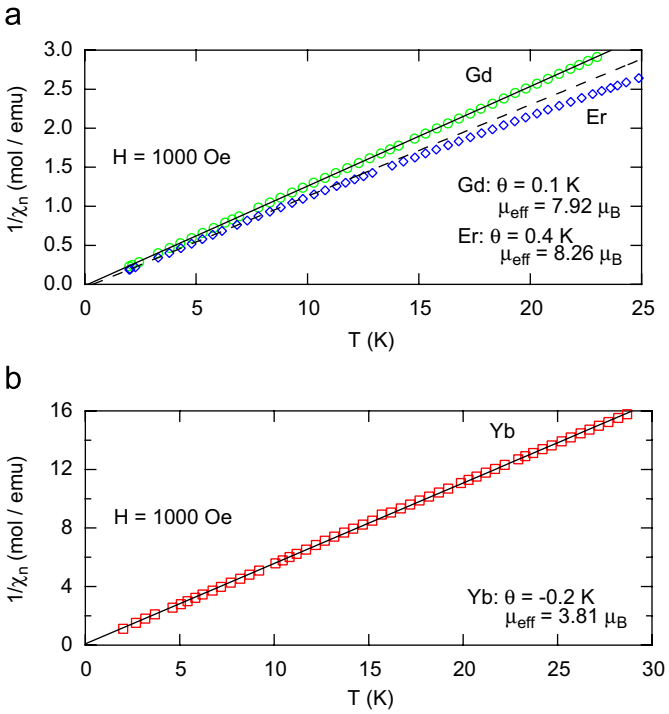

Fig. 10. Low-temperature inverse susceptibility plots emphasizing the magnetic properties of the ground state Stark level, as higher levels are thermally depopulated. The data were fit over the range in which they were linear: 2–20 K for $Gd(IO_3)_3$, 2–30 K for $Yb(IO_3)_3$, and 2–10 K for $Er(IO_3)_3$.

($\theta_{Er} = 0.4$ K, T_{offset} in χT plot $= +0.4$ K) is too large to be an experimental artifact, and represents very weak intrinsic ferromagnetic interactions. The behavior of Yb^{3+} ($\theta = -0.2$ K, $T_{offset} = 0$ K) indicates that its spins are either non-interacting or very weakly interacting.

4. Conclusion

This study reports on the properties of three f-element iodates, $Ln(IO_3)_3$ (Ln = Gd, Er, Yb). All three compounds exist in the $Bi(IO_3)_3$ structure type. Raman spectroscopy has been used to characterize $Gd(IO_3)_3$ and $Er(IO_3)_3$. It has been shown that Raman profiles can be used to distinguish between different families of iodate materials. Magnetization measurements of $Ln(IO_3)_3$ (Ln = Gd, Er, Yb) have also been investigated from 2 to 300 K. For $Gd(IO_3)_3$, the magnetic measurements indicate that Gd^{3+} exhibits its full 7.9 μ_B Hund's rule moment. In $Er(IO_3)_3$ and $Yb(IO_3)_3$, Er^{3+} and Yb^{3+} exhibited ground state moments and gap energy scales of 8.3 μ_B/70 K and 3.8 μ_B/160 K, respectively. Er^{3+} ions in $Er(IO_3)_3$ exhibited extremely weak ferromagnetic correlations (+0.4 K), while the magnetic ions in $Gd(IO_3)_3$ and $Yb(IO_3)_3$ were fully non-interacting within the resolution of our measurements (~0.2 K).

Acknowledgment

We are very grateful to Brian Sales and Ted Barnes for sharing their insights into f-electron magnetism, and to Yuri Janssen for his critical reading of the magnetic portion of this manuscript. The support for this work was provided by the Division of Chemical Sciences, Geosciences and Biosciences, OBES, USDOE, under Contract DE-AC05-00OR22725 with Oak Ridge National Laboratory, managed by UT-Battelle, LLC. Dr. Radu Custelcean and

Dr. Bruce Moyer are thanked for their generous allocation of X-ray diffractometer time, and also thanks go to David Mandrus for providing time on the SQUID magnetometer.

References

[1] S. Kaizaki, Coordin. Chem. Rev. 250 (2006) 1804.
[2] C. Pique, J.A. Blanco, R. Burriel, E. Abad, M. Artigas, M.T. Fernandez-Diaz, Phys. Rev. B 75 (2007) 224424.
[3] F. Pointillar, K. Bernot, R. Sessoli, D. Gatteschi, Chem. Eur. J. 13 (2007) 1602.
[4] I. Tereshina, S. Nikitin, W. Suski, J. Stepien-Damm, W. Iwasieczko, H. Drulis, K. Skokov, J. Alloys Compds. 404 (2005) 172.
[5] H. Cui, T. Otsuka, A. Kobayashi, N. Takeda, M. Ishikawa, Y. Misaki, H. Kobayashi, Inorg. Chem. 42 (2003) 6114.
[6] T. Kido, Y. Ikuta, Y. Sunatsuki, Y. Ogawa, N. Matsumoto, N. Re, Inorg. Chem. 42 (2003) 398.
[7] J.-P. Costes, F. Nicodème, Chem. Eur. J. 8 (2002) 3442.
[8] J.-P. Costes, J.-M.C. Juan, F. Dahan, F. Nicodème, Dalton Trans. (2003) 1272.
[9] Z. He, E.-Q. Gao, Z.-M. Wang, C.-H. Yan, M. Kurmoo, Inorg. Chem. 44 (2005) 862.
[10] J.-P. Costes, J.M. Clemente-Juan, F. Dahan, F. Nicodème, M. Verelst, Angew. Chem. Int. Ed. 41 (2002) 323.
[11] (a) R. Hedinger, M. Ghisletta, K. Hegeschweiler, E. Toth, A.E. Merbach, R. Sessoli, D. Gatteschi, V. Gramlich, Inorg. Chem. 37 (1998) 6698;
(b) A. Panagiotopoulos, T.F. Zafiropoulos, S.P. Perlepes, E. Bakalbassis, I. Masson-Ramade, O. Kahn, A. Terzis, C.P. Raptopoulou, Inorg. Chem. 34 (1995) 4918.
[12] M. Hernández-Molina, C. Ruiz-Pérez, T. López, F. Lloret, M. Julve, Inorg. Chem. 42 (2003) 5456.
[13] L.E. Roy, T. Hughbanks, J. Am. Chem. Soc. 128 (2006) 568.
[14] R.T. Macaluso, J.N. Millican, S. Nakatsuji, H.-O. Lee, B. Carter, N.O. Moreno, Z. Fisk, J.Y. Chan, J. Solid State Chem. 178 (2005) 3547.
[15] J.L. Sarrao, L.A. Morales, J.D. Thompson, B.L. Scott, G.R. Stewart, F. Wastin, J. Rebizant, P. Boulet, E. Colineau, G.H. Lander, Nature 420 (2002) 297.
[16] R.E. Sykora, L. Deakin, A. Mar, L. Soderholm, S. Skanthakumar, T.E. Albrecht-Schmitt, Chem. Mater. 16 (2004) 1343.
[17] Z. Assefa, J. Ling, R.G. Haire, T.E. Albrecht-Schmitt, R.E. Sykora, J. Solid State Chem. 179 (2006) 3653.
[18] R.E. Sykora, Z. Assefa, R.G. Haire, T.E. Albrecht-Schmitt, Inorg. Chem. 44 (2005) 5667.
[19] R.E. Sykora, Z. Assefa, R.G. Haire, T.E. Albrecht-Schmitt, J. Solid State Chem. 177 (2004) 4413.
[20] R.E. Sykora, Z. Assefa, R.G. Haire, T.E. Albrecht-Schmitt, Inorg. Chem. 45 (2006) 475.
[21] T.C. Shehee, R.E. Sykora, K.M. Ok, P.S. Halasyamani, T.E. Albrecht-Schmitt, Inorg. Chem. 42 (2003) 457.
[22] (a) P. Douglas, A.L. Hector, W. Levason, M.E. Light, M.L. Matthews, M. Webster, Z. Anorg. Allg. Chem. 630 (2004) 479;
(b) A.L. Hector, S.J. Henderson, W. Levason, M. Webster, Z. Anorg. Allg. Chem. 628 (2002) 198.
[23] (a) D. Phanon, A. Mosset, I. Gautier-Luneau, J. Mater. Chem. 17 (11) (2007) 1123;
(b) D. Phanon, A. Mosset, I. Gautier-Luneau, Solid State Sci. 9 (6) (2007) 496.
[24] W. Runde, A.C. Bean, L.F. Brodnax, B.L. Scott, Inorg. Chem. 45 (2006) 2479.
[25] X. Chen, X. Chang, H. Zang, Q. Wang, W. Xiao, J. Alloys Compds. 396 (2005) 255.
[26] R. Liminga, S.C. Abrahams, J.L. Bernstein, J. Chem. Phys. 67 (1977) 1015.
[27] S.C. Abrahams, J.L. Bernstein, K. Nassau, J. Solid State Chem. 16 (1976) 173.
[28] S.C. Abrahams, J.L. Bernstein, J. Chem. Phys. 69 (1978) 2505.
[29] N.T. Bagraev, D.M. Daraseliya, D.L. Dzhaparidze, V.V. Romanov, T.I. Sanadze, Fizika Tverdogo Tela 32 (1990) 2814.
[30] SADABS, Acta Crystallogr. A 51 (1995) 33.
[31] G.M. Sheldrick, SHELTXL PC, Version 5.0, An Integrated System for Solving, Refining, and Displaying Crystal Structures from Diffraction Data, Siemens Analytical X-ray Instruments, Inc., Madison, WI, 1994.
[32] B. Bentria, D. Benbertal, M. Bagieu-Beucher, R. Masse, A. Mosset, J. Chem. Crystallogr. 33 (2003) 867.
[33] X. Chen, H. Xue, X. Chang, H. Zang, W. Xiao, J. Alloys Compds. 398 (2005) 173.
[34] (a) I.D. Brown, D. Altermatt, Acta Crystallogr. B 41 (1985) 244;
(b) N.E. Brese, M. O'Keeffe, Acta Crystallogr. B 47 (1991) 192.
[35] R.E. Sykora, K.M. Ok, P.S. Halasyamani, T.E. Albrecht-Schmitt, J. Am. Chem. Soc. 124 (2002) 1951.
[36] N. Ngo, K. Kalachnikova, Z. Assefa, R.G. Haire, R.E. Sykora, J. Solid State Chem. 179 (2006) 3824.
[37] R. Liminga, S.C. Abrahams, J.L. Bernstein, J. Chem. Phys. 62 (1975) 755.
[38] G. Pracht, N. Lange, H.D. Lutz, Thermochim. Acta 293 (1997) 13.
[39] Th. Kellersohn, E. Alici, D. Eber, H.D. Lutz, Z. Kristallogr. 203 (1993) 225.
[40] A.C. Bean, B.L. Scott, T.E. Albrecht-Schmitt, W. Runde, Inorg. Chem. 42 (2003) 5632.
[41] V. Schellenschlager, G. Pracht, H.D. Lutz, J. Raman Spectrosc. 32 (2001) 373.
[42] H.D. Lutz, E. Suchanek, Spectrochim. Acta 56 (Part A) (2000) 2707.
[43] M.A. Ruderman, C. Kittel, Phys. Rev. 96 (1954) 99.
[44] K.W.H. Stevens, Magnetic Ions in Crystals, Princeton University Press, Princeton, 1997.
[45] J.M. O'Hare, V.L. Donlan, Phys. Rev. B 15 (1977) 10.
[46] Z. Mazurak, J.B. Gruber, J. Phys.: Condens. Matter 4 (1992) 3453.
[47] B.Z. Malkin, A.V. Vinokurov, J.M. Baker, J.M. Leask, M.G. Robinson, C.A. Hutchison, Proc.: Math. Phys. Eng. Sci. 452 (1996) 2509.
[48] B.Z. Malkin, A.R. Zkirov, M.N. Popova, S.A. Klimin, E.P. Chukalina, E. Antic-Fidancev, P. Goldner, P. Aschehoug, Phys. Rev. B 70 (2004) 075112.
[49] C. Li, C. Wyon, R. Mocorgé, IEEE J. Quant. Electron. 28 (1992) 1209.
[50] X. Mateos, M. Cinta Pujol, F. Güell, M. Galán, R. Maria Solé, J. Gavaldà, M. Aguiló, J. Massons, F. Díaz, IEEE J. Quant. Electron. 40 (2004) 759.
[51] J. Gruber, B. Zandi, L. Merkle, J. Appl. Phys. 83 (1998) 1009.